

Closer to critical resting-state neural dynamics in individuals with higher fluid intelligence

Takahiro Ezaki^{a,b}, Elohim Fonseca dos Reis^c, Takamitsu Watanabe^{d,e}, Michiko Sakaki^{f,g}, and Naoki Masuda^{c,h,i,*}

^aPRESTO, Japan Science and Technology Agency, Kawaguchi, Saitama, Japan

^bResearch Center for Advanced Science and Technology, The University of Tokyo, Meguro-ku, Tokyo, Japan

^cDepartment of Engineering Mathematics, University of Bristol, Clifton, Bristol, United Kingdom

^dInstitute of Cognitive Neuroscience, University College London, 17 Queen Square, London, WC1N 3AZ, United Kingdom

^eRIKEN Center for Brain Science, Wako, Saitama, Japan

^fSchool of Psychology and Clinical Language Sciences, University of Reading, Earley Gate, Whiteknights Road, Reading, United Kingdom

^gResearch Institute, Kochi University of Technology, Kami, Kochi, Japan

^hDepartment of Mathematics, University at Buffalo, State University of New York, Buffalo, New York, USA

ⁱComputational and Data-Enabled Science and Engineering Program, University at Buffalo, State University of New York, Buffalo, New York, USA

*naokimas@buffalo.edu

ABSTRACT

According to the critical brain hypothesis, the brain is considered to operate near criticality and realize efficient neural computations. Despite the prior theoretical and empirical evidence in favor of the hypothesis, no direct link has been provided between human cognitive performance and the neural criticality. Here we provide such a key link by analyzing resting-state dynamics of functional magnetic resonance imaging (fMRI) networks at a whole-brain level. We develop a data-driven analysis method, inspired from statistical physics theory of spin systems, to map out the whole-brain neural dynamics onto a phase diagram. Using this tool, we show evidence that neural dynamics of human participants with higher fluid intelligence quotient scores are closer to a critical state, i.e., the boundary between the paramagnetic phase and the spin-glass (SG) phase. The present results are consistent with the notion of “edge-of-chaos” neural computation.

Introduction

Critical brain hypothesis posits that the brain operates near a critical regime, i.e., boundary between different phases showing qualitatively different behaviors^{1–6}. This hypothesis has been investigated for more than two decades including criticisms such as the presence of alternative mechanisms explaining power law scaling in the relevant observables^{7–10}. Experimental evidence such as the recovery of critical behavior after interventions, which is difficult to explain by alternative mechanisms, lends supports to the hypothesis⁹.

Theoretical and experimental work has shown that neural systems operating near criticality are advantageous in information transmission, information storage, classification, and nonlinear input filtering^{1,3,5,11–14}. These findings align with the idea of edge-of-chaos computation, with which computational ability of a system is maximized at a phase transition between a chaotic phase and a non-chaotic phase^{15–17}. These findings are also in line with a general contention that cognitive computations occur as neural dynamical processes^{18,19}.

A prediction from the critical brain hypothesis is that neural dynamics in individuals with higher cognitive abilities should be closer to criticality than in those with lower cognitive abilities. However, whether high cognitive skills are associated with criticality has not been empirically proven. In fact, recent emerging evidence suggests that human cognitive performance is associated with appropriate transitions between relatively discrete brain states during rest^{20–22}, working memory tasks²³ and visual perception tasks²⁴. Furthermore, these and other studies^{18,19,25} support that state-transition dynamics in the brain involve large-scale brain networks. These arguments are consistent with the proposal that many cognitive functions seem to depend on network connectivity among various regions scattered over the whole brain²⁶. On these grounds, in the present study we hypothesize that complex and transitory neural dynamics of the brain network (i.e., dynamic transitions among discrete brain states) that are close to criticality are associated with high cognitive performance of humans.

Two major conventional methods for examining criticality and edge-of-chaos computation in empirical neural data are not capable of testing this hypothesis for their own reasons. First, many of the experimental studies testing the critical brain hypothesis have examined neuronal avalanches^{11,12}, including the case of humans^{5,27,28}. Neuronal avalanches are bursts of cascading activity of neurons, whose power-law properties have been related to criticality. However, studies of neuronal avalanches have focused on their scale-free dynamics in space and time, with which statistics of avalanches obey power laws. Scale-free dynamics of neuronal avalanches is a question orthogonal to patterns of transitions between discrete states. Second, nonlinear time series analysis has found that electroencephalography (EEG) signals recorded from the brains of healthy controls are chaotic and that the degree of chaoticity is stronger for healthy controls than individuals with, for example, epilepsy, Alzheimer's disease, and schizophrenia²⁹. However, this method is not usually for interacting time series. Therefore, it does not directly reveal how different brain regions interact or whether possible critical or chaotic dynamics are an outcome of the dynamics at a single region or interaction among different regions.

In the present study, we develop a data-driven method to measure the extent to which neural dynamics obtained from large-scale brain networks are close to criticality and complex state-transition dynamics. The method stands on two established findings. First, statistical mechanical theory of the Ising spin-system model posits that the so-called spin-glass phase corresponds to rugged energy landscapes (and therefore, complex state-transition dynamics)³⁰ and chaotic dynamics^{31–33}. Therefore, we are interested in how close the given data are to dynamics in the spin-glass phase. Second, the Ising model has been fitted to various electrophysiological data^{6,34–36} and fMRI data recorded from a collection of regions of interest (ROIs)^{20,21,24,37,38} during rest or tasks with a high accuracy. Therefore, we start by fitting the Ising model to the multivariate fMRI data. Then, we draw phase diagrams of functional brain networks at a whole-brain level. By construction, the dynamical behavior of the system is qualitatively distinct in different phases. The method determines the location of a brain in the phase diagram and thus tells us whether the large-scale brain dynamics of individual participants are ordered, disordered or chaotic (i.e. spin-glass) dynamics as well as how close the dynamics are to a phase transition curve, on which the system shows critical behavior.

We deploy this method to resting-state fMRI data recorded from human adults with different intelligence quotient (IQ) scores. As a cognitive ability of interest, we focus on fluid intelligence, which refers to the ability to think logically and solve problems with a limited amount of task-related information³⁹. Fluid intelligence is strongly related to the general intelligence factor, g ³⁹ and predictive of real-world outcomes such as job performance⁴⁰. We examine our hypothesis that large-scale brain dynamics of individuals higher in the intelligence score that measures fluid intelligence are closer to critical.

Results

Brain dynamics are close to the spin-glass phase transition.

We first fitted the pairwise maximum entropy model (PMEM), which assumes pairwise interaction between ROIs and otherwise produces a maximally random distribution, which is a Boltzmann distribution. The PMEM is equivalent to the inverse Ising model, where the parameters of the Ising model are inferred from data. Because the model assumes binary data, we binarized the resting-state fMRI signals obtained from 138 healthy adults. The binarized activity pattern at $N (= 264)$ ROIs⁴¹ at time t ($t = 1, \dots, t_{\max}$; $t_{\max} = 258$) is denoted by $\mathbf{S}(t) = (S_1(t), \dots, S_N(t)) \in \{-1, +1\}^N$, where $S_i(t) = 1$ and $S_i(t) = -1$ ($i = 1, \dots, N$) indicate that ROI i is active (i.e., the fMRI signal is larger than a threshold) and inactive (i.e., smaller than the threshold), respectively. We fitted the following probability distribution to the population of the 138 participants by maximizing a pseudo likelihood (see Methods)^{24,34}:

$$P(\mathbf{S} | \mathbf{h}, \mathbf{J}) = \frac{\exp[-E(\mathbf{S} | \mathbf{h}, \mathbf{J})]}{\sum_{\mathbf{S} \in \{-1, 1\}^N} \exp[-E(\mathbf{S} | \mathbf{h}, \mathbf{J})]}. \quad (1)$$

In (1),

$$E(\mathbf{S} | \mathbf{h}, \mathbf{J}) = - \sum_{i=1}^N h_i S_i - \frac{1}{2} \sum_{i=1}^N \sum_{\substack{j=1 \\ j \neq i}}^N J_{ij} S_i S_j \quad (2)$$

is the energy of activity pattern \mathbf{S} , $\mathbf{h} = \{h_i : 1 \leq i \leq N\}$, and $\mathbf{J} = \{J_{ij} : 1 \leq i \neq j \leq N\}$, where $J_{ij} = J_{ji}$. Although we refer to E as the energy, E does not represent the physical energy of a neural system but is a mathematical construct representing the frequency with which activity pattern \mathbf{S} appears in the given data. Activity pattern \mathbf{S} appears rarely in the data if E corresponding to \mathbf{S} is large and vice versa. Parameter h_i represents the tendency that $S_i = 1$ is taken because a positive large value of h_i implies that $S_i = 1$ as opposed to $S_i = -1$ lowers the energy and hence raises the probability that \mathbf{S} with $S_i = 1$ appears. Parameter J_{ij} represents a functional connectivity between ROIs i and j because, if J_{ij} is away from 0, S_i and S_j would be correlated in general. We denote the estimated parameter values by $\hat{\mathbf{h}}$ and $\hat{\mathbf{J}}$.

Then, to evaluate how close the current data are to criticality, we drew phase diagrams by sweeping values of \mathbf{J} . In the phase diagrams, we fixed \mathbf{h} at $\hat{\mathbf{h}}$ following the theoretical convention³⁰, including when the PMEM is applied to data analysis⁶. We set $\mathbf{h} = \hat{\mathbf{h}}$ also because changing the \mathbf{h} values did not qualitatively change the phase diagrams (Supplementary Fig. 1). Then, we varied the mean μ and standard deviation σ of \mathbf{J} by linearly transforming \mathbf{J} , i.e.,

$$J_{ij} = (\hat{J}_{ij} - \hat{\mu}) \frac{\sigma}{\hat{\sigma}} + \mu. \quad (3)$$

In (3), $\hat{\mu} = 1.57 \times 10^{-3}$ and $\hat{\sigma} = 3.57 \times 10^{-2}$ are the mean and standard deviation of the off-diagonal elements of $\hat{\mathbf{J}}$ estimated for the empirical data. We chose the parametrization given in Eq. (3) motivated by the past investigation of the archetypical Sherrington-Kirkpatrick (SK) model of spin systems³⁰. The SK model, a type of Ising model, is defined with parameters J_{ij} ($1 \leq i \neq j \leq N$) that are independently drawn from the Gaussian distribution with the tunable mean and standard deviation and has extensively been studied for investigating the so-called spin-glass phase transition owing to its theoretical tractability. In the spin-glass phase, the system shows a disorderly frozen pattern of spins rather than uniform or periodic ones. For each set of J_{ij} values ($1 \leq i \neq j \leq N$) specified by a (μ, σ) pair, we performed Monte Carlo simulations and calculated observables (see Methods). In this manner, we generated a phase diagram for each observable in terms of μ and σ .

Two primary observables (called order parameters in physics literature) employed in studies of spin systems are the magnetization, denoted by m , and the spin-glass order parameter, denoted by q . The magnetization is defined by $m = \sum_{1 \leq i \leq N} \langle S_i \rangle / N$, where $\langle \cdot \rangle$ represents the ensemble average, and quantifies the mean tendency that $S_i = 1$ as opposed to $S_i = -1$ is taken across the ROIs. The spin-glass order parameter is defined by $q = \sum_{1 \leq i \leq N} \langle S_i^2 \rangle / N$ and represents the degree of local magnetization at individual ROIs. We show m and q as functions of μ and σ in Fig. 1a, b, respectively. The obtained phase diagrams were qualitatively the same as those for the SK model of the same system size, which was given by Eqs. (1) and (2) with each J_{ij} ($= J_{ji}, i \neq j$) being independently drawn from a Gaussian distribution with mean μ and standard deviation σ (Fig. 1e, f). The parameter space is composed of three qualitatively different phases³⁰. The paramagnetic phase, characterized by $m = 0$ and $q = 0$ in the limit of $N \rightarrow \infty$, represents the situation in which each S_i randomly flips between 1 and -1 , yielding no magnetization. The ferromagnetic phase, characterized by $m \neq 0$ and $q > 0$, represents the situation in which (almost) all S_i 's align in one direction (i.e., $S_i = 1$ or $S_i = -1$). The spin-glass (SG) phase, characterized by $m = 0$ and $q > 0$, represents the situation in which each S_i is locally magnetized but not globally aligned to a specific direction³⁰. Note that the finite size effect of our system blurred the boundaries between the different phases. The current data pooled across the participants lie in the paramagnetic phase and are close to the boundary to the SG phase (crosses in Fig. 1a, b). In theory, the spin-glass susceptibility, $\chi_{SG} = N^{-1} \beta^2 \sum_{1 \leq i, j \leq N} c_{ij}^2$, where $c_{ij} = \langle S_i S_j \rangle - m_i m_j$, diverges on the boundary between the paramagnetic and SG phases³⁰. The empirical data yielded a relatively large χ_{SG} value in the phase diagram (Fig. 1c). In contrast, we did not find a signature of phase transition in terms of the uniform susceptibility defined by $\chi_{uni} = N^{-1} \beta \sum_{1 \leq i, j \leq N} c_{ij}$, which characterizes the transition between the paramagnetic and ferromagnetic phases³⁰ (Fig. 1d). Note that the phase diagrams for χ_{SG} and χ_{uni} resemble those obtained from the SK model (Fig. 1g, h).

Next, we examined where brain activity patterns of each participant were located in the phase diagrams. We did so by finding the μ and σ values corresponding to the χ_{SG} and χ_{uni} values of each participant (see Methods). It should be noted that χ_{SG} and χ_{uni} can be calculated for each individual only from the covariance matrix of the data, without estimating the PMEM. The location of each participant in the phase diagram of χ_{SG} is shown by the circles in Fig. 1c. The cross section of this phase diagram for $\mu = \hat{\mu}$ (along the dashed line shown in Fig. 1c) is shown in Fig. 1i. We also projected the χ_{SG} values for the individual participants (circles in Fig. 1i) based on the value of σ estimated for each individual (circles in Fig. 1c). Figure 1i suggests that the empirical data are located in a range of σ that constitutes a peak, further confirming that the brain dynamics of the different participants are close to the paramagnetic-SG phase transition and to different extents. In contrast, the participants were far from the paramagnetic-ferromagnetic phase boundary. This is confirmed in Fig. 1j, which is a cross section of the phase diagram for χ_{uni} (along the dashed line shown in Fig. 1d) together with the χ_{uni} values for the single participants.

The χ_{SG} value for the individual participants was off the largest possible values in the phase diagram (Fig. 1i). To examine this point, we carried out a finite size scaling on χ_{SG} (Fig. 1k). To emulate systems of smaller sizes than $N = 264$, we selected N' out of the N ROIs uniformly at random and fitted the PMEM. The estimated parameter values are denoted by $\hat{\mathbf{h}}$ and $\hat{\mathbf{J}}$ without confusion. Then, we simulated the equilibrium state of the system by scanning \mathbf{J} according to (3), where we varied σ while fixing $\mu = \hat{\mu}$. In this manner, we sought to investigate how close the data were to the SG phase transition at each N' value. As shown in Fig. 1k, the peak value of χ_{SG} increased as N' increased, suggesting that the paramagnetic-SG phase transition is approached as the system size increases. In addition, the position of the peak, denoted by σ_{peak} , shifted toward the value for the empirical data, $\hat{\sigma}$, as N increased. By regressing $\sigma_{peak}/\hat{\sigma}$ linearly on $1/N'$ (inset of Fig. 1k), we estimated $\sigma_{peak}/\hat{\sigma} = 1.45 \pm 0.04$ in the limit $N' \rightarrow \infty$.

The performance IQ is associated with the criticality.

To test our hypothesis that criticality of brain dynamics is associated with human fluid intelligence, we examined the correlation between χ_{SG} , which encodes the proximity of each participant's neural dynamics to the paramagnetic-SG phase transition (Fig. 1c, i), and the performance IQ score. The performance IQ score is defined based on tasks that are reflective of fluid intelligence^{42,43}. An enlargement of Fig. 1c is shown in Fig. 2a, where the participants are shown in different colors depending on whether they have a higher performance IQ score (defined by the score value larger than or equal to the median, 109, $n = 68$) and a lower score ($n = 63$). We found that higher-IQ participants tended to be closer to the paramagnetic-SG phase transition than lower-IQ participants, as measured by σ ($t_{129} = 3.17, P < 0.002$, Cohen's $d = 0.55$ in a two-sample t -test). The results were qualitatively the same when the outliers were excluded ($t_{127} = 3.52, P < 10^{-3}, d = 0.62$). In contrast, the two groups were not different in terms of the distance to the paramagnetic-ferromagnetic phase transition as measured by μ ($t_{129} = 0.77, P = 0.44, d = 0.13$ with the outlier included; $t_{127} = 0.85, P = 0.40, d = 0.15$ with the outlier excluded).

More systematically, we found a mild positive correlation between χ_{SG} and the performance IQ score ($r_{129} = 0.24, P_{\text{Bonferroni}} = 0.011$; also see Fig. 2b). However, the verbal IQ score, which is based on individuals' verbal knowledge^{42,43}, was not correlated with χ_{SG} ($r_{126} = 0.06, P_{\text{uncorrected}} = 0.50$, Fig. 2c). The correlation between χ_{SG} and the performance IQ score was also significantly larger than the correlation between χ_{SG} and the verbal IQ score ($t_{121} = 2.33, P = 0.021$, in the Williams t -test for comparing two nonindependent correlations with a variable in common⁴⁴). These results suggest that the criticality of brain dynamics plays more roles in fluid intelligence than when simply retrieving verbal knowledge. Note that we partialled out the effects of the age and gender in this and the following analysis unless we state otherwise.

The correlation between the full IQ score^{42,43} and χ_{SG} was intermediate between the results for the performance and verbal IQ scores ($r_{130} = 0.19, P = 0.026$; also see Fig. 2d), which is natural because the performance and verbal IQ scores are components of the full IQ score.

The association between the spin-glass susceptibility, χ_{SG} , and the different types of IQ scores was robust in the following four ways. First, the exclusion of the two outliers determined by Tukey's 1.5 criteria⁴⁵ did not affect the significance of the results (χ_{SG} vs performance IQ: $r_{127} = 0.27, P_{\text{Bonferroni}} = 0.005$; χ_{SG} vs verbal IQ: $r_{124} = 0.13, P_{\text{Bonferroni}} = 0.27$; χ_{SG} vs full IQ: $r_{128} = 0.25, P = 0.005$). Second, the results were robust against variation on the threshold value for binarizing the fMRI signal (Supplementary Fig. 2). Furthermore, changes in the threshold value did not substantially alter the phase diagrams (Supplementary Fig. 3). Third, the results were preserved even when the global signal (see Methods) was not subtracted from the fMRI signals (χ_{SG} vs performance IQ: $r_{129} = 0.22, P_{\text{Bonferroni}} = 0.02$; χ_{SG} vs verbal IQ: $r_{126} = 0.046, P_{\text{uncorrected}} = 0.61$; χ_{SG} vs full IQ: $r_{130} = 0.18, P = 0.043$; the outliers were not removed). Fourth, we did not find a gender difference in the correlation coefficient between χ_{SG} and the IQ scores (performance IQ: $Z = 0.33, P = 0.74$ in a Z -test for a pair of correlation coefficients⁴⁶; verbal IQ: $Z = 0.43, P = 0.67$; full IQ: $Z = 0.17, P = 0.86$). In this gender-difference analysis, we partialled out the effect of the age but not the gender.

Irrelevance of the paramagnetic-ferromagnetic transition.

The IQ was not correlated with χ_{uni} (performance IQ: $r_{129} = 0.10, P_{\text{uncorrected}} = 0.27$; verbal IQ: $r_{126} = 0.093, P_{\text{uncorrected}} = 0.30$; full IQ: $r_{130} = 0.10, P = 0.24$, each test including the outliers; performance IQ: $r_{124} = 0.013, P_{\text{uncorrected}} = 0.89$; verbal IQ: $r_{121} = 0.039, P_{\text{uncorrected}} = 0.67$; full IQ: $r_{125} = 0.020, P = 0.82$, each test excluding the outliers). The specific heat (denoted by C ; see Methods for definition) was only mildly correlated with the performance IQ score (performance IQ: $r_{129} = 0.21, P_{\text{Bonferroni}} = 0.034$; verbal IQ: $r_{126} = -0.0056, P_{\text{uncorrected}} = 0.95$; full IQ: $r_{130} = 0.13, P = 0.14$, each test including the outliers; performance IQ: $r_{125} = 0.16, P_{\text{uncorrected}} = 0.08$; verbal IQ: $r_{122} = -0.016, P_{\text{uncorrected}} = 0.86$; full IQ: $r_{126} = 0.10, P = 0.26$, each test excluding the outliers). Because χ_{uni} and C diverge in the paramagnetic-ferromagnetic phase transition but not in the paramagnetic-SG phase transition³⁰, these negative results lend another support to the relevance of the SG phase rather than the ferromagnetic phase to intelligence.

Consistency with the critical slowing down analysis.

The previous literature used various measures of criticality. We measured for each participant such a measure, i.e., the scaling exponent of autocorrelation^{47,48}. This measure quantifies the critical slowing down phenomenon, which has been observed in critical states of the brain⁴⁸. Note that this index quantifies temporal correlation and is orthogonal to what we have measured. We computed the scaling exponent for the autocorrelation function of the fMRI signal at each ROI, using the detrended fluctuation analysis^{47,48}. Then, we took the average of the scaling exponent over the $N = 264$ ROIs for each participant, which is denoted by α . The association between α and the IQ scores was consistent with the results for χ_{SG} (α vs performance IQ: $r_{129} = 0.29, P_{\text{Bonferroni}} = 0.002$; α vs verbal IQ: $r_{126} = 0.19, P_{\text{Bonferroni}} = 0.068$; α vs full IQ: $r_{130} = 0.25, P = 0.003$). These results were robust against the removal of outliers (α vs performance IQ: $r_{128} = 0.28, P_{\text{Bonferroni}} = 0.002$; α vs verbal IQ: $r_{125} = 0.17, P_{\text{Bonferroni}} = 0.10$; α vs full IQ: $r_{130} = 0.25, P = 0.003$).

We then performed a multivariate linear regression of the performance IQ with χ_{SG} and α being the independent variables. We found a significant regression equation ($F_{2,128} = 8.0, P < 0.001$, adjusted $R^2 = 0.11$). Both χ_{SG} and α were significantly

correlated with the performance IQ (χ_{SG} : $\beta = 0.18$, $P = 0.039$; α : $\beta = 2.4$, $P = 0.0067$). This result implies that the association between χ_{SG} and the performance IQ that we have found is not a byproduct of that between α and the performance IQ. The variance inflation factor for both independent variables was equal to 1.07; this value is small enough for justifying the use of the multivariate regression.

Effects of data length and individual variability.

We examined if the limited data length and between-participant variability in our data influenced our results. First, we investigated how the estimation of the individual participant's χ_{SG} and χ_{uni} depended on the length of her/his fMRI data (Supplementary Fig. 4a). The results were qualitatively the same as those obtained with all the data if we used approximately more than two thirds of the data (i.e., number of volumes per participant larger than ≈ 150). The correlation between χ_{SG} and the IQ scores and that between χ_{uni} and the IQ scores were also preserved with the aforementioned data length (Supplementary Fig. 4b, c). Therefore, our main results based on the χ_{SG} and χ_{uni} are considered to be reliable in terms of the data length.

Second, as we did in our previous studies^{21,37}, we divided the participants into two subgroups of the same size and ran some of the main analyses for the subgroups. We started by comparing the pairwise activity correlation, $\langle S_i S_j \rangle$, for each (i, j) pair between the two subgroups. The $\langle S_i S_j \rangle$ values were strongly correlated between the subgroups and also between the empirical data and estimated PMEMs for the two subgroups (Supplementary Fig. 5). We further confirmed that the phase diagrams were similar between the two subgroups (Supplementary Fig. 6). Moreover, we estimated $\tilde{\mu}$ and $\tilde{\sigma}$ for each participant only using the subgroup of participants to which the focal participant belongs. The results were similar to those estimated based on all the participants (Supplementary Fig. 7). Therefore, we conclude that the estimation of the phase diagrams (Fig. 1a–h) and their derivatives (i.e., $\tilde{\mu}$ and $\tilde{\sigma}$), which are based on the estimated phase diagrams, are robust enough against fluctuations in data, such as those caused by a reduced number of participants.

Discussion

We provided empirical support that neural dynamics of humans with higher intellectual ability are closer to critical. The present results are consistent with the standing claim of the “critical brain hypothesis” and “edge-of-chaos computation”, which jointly dictate that the brain is maximizing its computational performance by poising its dynamics close to the criticality, particularly the criticality involving a chaotic regime.

Here we presented an explicit, albeit only moderate, correlation between the IQ scores and the distance from criticality at an individual's level. Human intelligence has been shown to be associated with genetic factors, brain size, the volume of specific brain regions⁴⁹, and the structure of brain networks^{26,49}. The present results derived from dynamic fMRI signals provide an orthogonal account of human intelligence as compared to these previous studies and are consistent with the view that cognition is a dynamical process linked to neural dynamics^{18,19}.

A previous study showed that sleep deprivation pulls the brain dynamics away from the criticality⁵⁰. This result is consistent with ours because sleep deprivation generally compromises one's cognitive and intellectual functions⁵¹.

Previous studies showed that the functional connectivity between particular pairs of ROIs or between subsystems of the brain in the resting state was correlated with intellectual ability^{49,52}. These previous results are consistent with ours in the sense that the SG susceptibility can be regarded as the square sum of a type of functional connectivity over the pairs of ROIs and the intellectual score was positively correlated with the SG susceptibility in our analysis. In contrast to these previous studies, which looked at individual connectivity between two regions or subnetworks, we considered $N = 264$ ROIs scattered over the brain⁴¹ as a single functional network. We took this approach for two reasons. First, intelligence is considered to depend on large-scale brain networks^{26,52–54}. Second, phase diagram analysis ideally requires a thermodynamic limit, i.e., infinitely many ROIs. One strategy to further approach the thermodynamic limit is to use a single voxel acquired by MRI as a node, significantly scaling up N . In this case, spatial correlation among ROIs, which we have ignored in the present study, would be prominent. Because the spatial dimensionality affects the phase diagrams even qualitatively³⁰, this case may require two- or three-dimensional SG models. We leave this as a future problem. The literature also suggest that specific brain systems such as the fronto-parietal network⁵⁵ and the default-mode network⁵⁶ predict intelligence of humans. Running the same analysis for these and other brain systems to seek specificity of the results warrants future work. Because the present method requires hundreds of ROIs, we may benefit from considering voxel-wise networks of a specific brain system that allow many ROIs for particular brain systems.

In our previous paper, we posed the limited accuracy of fitting the PMEM to fMRI data when N is large³⁸. The argument was based on the probability that each of the 2^N possible activity patterns appears compared between the empirical data and the estimated PMEM. In the present manuscript, we have not used this accuracy measure, because it cannot be calculated when N is large. Instead, we validated the model by confirming that the difference between the empirical data and estimated PMEM in terms of the signal average, $\langle S_i \rangle$, and the pairwise correlation, $\langle S_i S_j \rangle$, is small (Supplementary Fig. 8). This approach is based on the assumption that the average and second order correlation of signals explain most of the information contained in the

given data, which has been confirmed for smaller N in previous studies using fMRI data^{21,24,37,38}. Although only comparing $\langle S_i \rangle$ and $\langle S_i S_j \rangle$ between the data and model is a weaker notion of accuracy of fit than using the accuracy measure³⁸, the former approach has widely been accepted, explicitly or implicitly, in the literature^{57,58}. However, we point out that how to justify the use of PMEMs when N is large remains an open issue.

There are various types of criticality, corresponding to different types of phase transitions. Within the framework of the Ising model, we showed that human fMRI data were in the paramagnetic phase and were close to the boundary with the SG phase but not to the boundary with the ferromagnetic phase. Furthermore, high fluid intelligence was associated with the proximity to the boundary between the paramagnetic and SG phases. In theory, the SG phase yields chaotic dynamics in spin systems including the SK model^{31–33}, whereas the ferromagnetic phase is obviously non-chaotic. Therefore, although the definition of the chaos in the SG phase is different from that observed in cellular automata¹⁵ and recurrent neural networks^{16,17}, our results are consistent with the idea of enhanced computational performance at the edge of chaos.

The previous accounts of the critical brain or critical neural circuits are mostly concerned with phase transitions different from the paramagnetic-SG phase transition or its analogues. Examples include phase transitions between quiescent (i.e., subcritical) and active (i.e., supercritical) phases as an excitability control parameter changes^{11,12,59–61}, between ordered and chaotic phases as connectivity parameters change¹⁷, between a low-activity monostable state and a high-activity multistable state⁶², and the divergence of heat capacity^{5,6,35,36}. Note that, in the theory of the Ising models, the heat capacity diverges on the boundary between the paramagnetic and ferromagnetic phases, whereas it increases without diverging on the boundary between the paramagnetic and SG phases³⁰. Most of these previous results based on the Ising model related neural dynamics to the paramagnetic-ferromagnetic phase transition rather than the paramagnetic-SG transition. Roughly speaking, paramagnetic and ferromagnetic phases correspond to active and quiescent phases, respectively. Computational studies also support the ferromagnetism^{13,63,64}. In contrast, we provided a signature of the paramagnetic-SG phase transition, not the paramagnetic-ferromagnetic transition. Fraiman *et al.* reported that the Ising model at the paramagnetic-ferromagnetic phase transition explains properties of functional networks based on fMRI data⁶³. They used a two-dimensional Ising model with a uniform strength of interaction between pairs of nodes that are adjacent on a square lattice (and $J_{ij} = 0$ for the rest of pairs). Another study that suggested the paramagnetic-ferromagnetic phase transition for fMRI signals also assumed a uniform J_{ij} ⁶⁴. In contrast, we did not constrain the J_{ij} values and instead inferred the J_{ij} values (i.e., structure of functional network) using the PMEM. Because these previous studies^{63,64} did not assume heterogeneity in J_{ij} as we did, their results do not contradict ours. In fact, the assumption of a uniform J_{ij} corresponds to setting $\sigma = 0$ in our phase diagrams. If one varies μ under the condition $\sigma = 0$, the only possible phase transition is the paramagnetic-ferromagnetic transition (Fig. 1a–d). However, that phase transition point, which is derived under the condition $\sigma = 0$, is far from the location of the empirical data when σ is allowed to deviate from 0 (crosses in Fig. 1a–d). Therefore, allowing heterogeneity in J_{ij} may be key to further clarifying the nature of critical neural dynamics.

We showed that neural dynamics for each participant were close to but substantially off the criticality separating the paramagnetic and SG phases. Other studies using the PMEM⁶⁵ and other models⁶⁶ also support off-critical as opposed to critical neural dynamics in the brain. A study applying the PMEM to local field potentials suggested that such off-critical dynamics may potentially have functional advantages because the off-critical situation would prevent the dynamics to get past the phase boundary to enter the other phase under the presence of noise⁶⁶. The other phase may correspond to pathological neural dynamics such as epilepsy. The off-critical neural dynamics that we found for our participants, regardless of their IQ scores, may benefit from the same functional advantage.

Applying the current analysis pipeline to various neuroimaging and electrophysiological data in different contexts, from health to disease, and during rest and tasks, to evaluate the relevance of the different types of phase transitions warrants future work. For example, as a disease progresses, the brain dynamics may be gradually altered to transit from one phase to another, or to approach or repel from a phase transition curve. In fact, the method is applicable to general multivariate time series. Deployment of the present method to other biological and non-biological data may also be productive.

One could classify the data from participants with high and low IQ scores using a simple multivariate Gaussian decoder⁶⁷. Such a decoder would assume as input the mean and covariance of the fMRI data for each participant or its random samples having the same mean and covariance. In fact, multivariate Gaussian distributions having the same covariance structure as the empirical data yielded similar results (Supplementary Fig. 9). Because our PMEM also assumed the same input but was not optimized for classifying the participants, an optimized Gaussian decoder will probably be more efficient than our PMEM in explaining the IQ scores of the participants. This approach is conceptually much simpler than the present one, which employ the PMEM and its phase diagrams. However, the aim of the present study was to find empirical support of the critical brain hypothesis by relating the fMRI data to the phase diagrams of an archetypal spin system rather than to efficiently classify participants.

We found that the SG susceptibility was positively, although not strongly, correlated with individual differences in the performance IQ score but not in the verbal IQ score. The verbal IQ reflects individuals' knowledge about verbal concepts and

crystalized intelligence⁴³; crystalized intelligence refers to one's cognitive functioning associated with previously acquired knowledge and skills. In contrast, the performance IQ reflects fluid intelligence, which refers to active or effortful problem solving and maintenance of information³⁹. Our results imply that the critical brain dynamics may be particularly useful for active and flexible cognitive functions.

Methods

Participants.

One-hundred thirty eight ($n = 138$) healthy and right-handed adult participants (54 females and 84 males) in the Nathan Kline Institute's (NKI) Rockland phase I Sample⁶⁸ were analyzed. The data collection was approved by the institutional review board of the Nathan Kline Institute (no. 226781). Written informed consent was obtained for all the participants. Although the data set contains a wide range of the age (18-85 yo), the present results were not an age effect because the IQ values are standardized for age⁴² and because we have partialled out the effect of age (and the gender) in the present analysis. Participants' IQ scores were derived from the Wechsler Abbreviated Scale of Intelligence (WASI)⁴². We used the full scale IQ (full IQ for short), performance IQ, and verbal IQ.

Preprocessing.

We used the same MRI data and the same preprocessing pipeline as our previous study's⁶⁹, except that we used resting-state fMRI signals from 264 ROIs, whose coordinates were derived in the previous literature⁴¹. In short, we submitted the resting-state fMRI data in the NKI Rockland phase I Sample with TR=2500 ms and for 10 m 55 s for each participant to our preprocessing pipeline in FSL and applied band-pass temporal filtering (0.01–0.1 Hz).

The obtained fMRI signals $x_i(t)$ ($i = 1, \dots, N; t = 1, \dots, t_{\max}$, where $t_{\max} = 258$) were transformed into their z-values using $z_i(t) = (x_i(t) - \mu(x(t))) / \sigma(x(t))$, where $\mu(x(t))$ and $\sigma(x(t))$ represent the average and standard deviation of $x_i(t)$ over the N ROIs, respectively. Note that $\mu(x(t))$ is the global signal. When we tested the robustness of the results by not removing the global signal, we set $z_i(t) = x_i(t)$. We binarized the signal as follows:

$$S_i(t) = \begin{cases} +1 & \text{if } z_i(t) \geq 0, \\ -1 & \text{if } z_i(t) < 0. \end{cases} \quad (4)$$

Estimation of \mathbf{h} and \mathbf{J} by pseudo-likelihood maximization.

The probability of each of the 2^N activity patterns is equal to its frequency of occurrence normalized by the t_{\max} time points and 138 participants. We fitted the Ising model to this probability distribution on the 2^N activity patterns.

We estimated the parameter values of the Ising model (i.e., \mathbf{h} and \mathbf{J}) by maximizing a pseudo-likelihood (PL)^{38,70}. We approximate the likelihood function by

$$\mathcal{L}(\mathbf{h}, \mathbf{J}) \approx \prod_{t=1}^{t_{\max}} \prod_{i=1}^N \tilde{P}(S_i | \mathbf{h}, \mathbf{J}, \mathbf{S}_{/i}(t)), \quad (5)$$

where \tilde{P} represents the conditional Boltzmann distribution for a single spin, $S_i \in \{-1, 1\}$, when the S_j values ($j \neq i$) are equal to $\mathbf{S}_{/i}(t) \equiv (S_1(t), \dots, S_{i-1}(t), S_{i+1}(t), \dots, S_N(t))$, i.e.,

$$\tilde{P}(S_i | \mathbf{h}, \mathbf{J}, \mathbf{S}_{/i}(t)) = \frac{\exp \left[h_i S_i + \sum_{\substack{j=1 \\ j \neq i}}^N J_{ij} S_i S_j(t) \right]}{\sum_{S'_i=-1, +1} \exp \left[h_i S'_i + \sum_{\substack{j=1 \\ j \neq i}}^N J_{ij} S'_i S_j(t) \right]}. \quad (6)$$

In Eq. (6), one determines the probability of each activity pattern under the assumption that S_j ($j \neq i$) does not change when drawing the value of S_i ($i = 1, \dots, N$). We ran a gradient ascent updating scheme given by

$$h_i^{\text{new}} - h_i^{\text{old}} = \varepsilon (\langle S_i \rangle_{\text{empirical}} - \langle \bar{S}_i \rangle_{\tilde{P}}), \quad (7)$$

$$J_{ij}^{\text{new}} - J_{ij}^{\text{old}} = \varepsilon (\langle S_i S_j \rangle_{\text{empirical}} - \langle \bar{S}_i \bar{S}_j \rangle_{\tilde{P}}), \quad (8)$$

where $\langle S_i \rangle_{\tilde{P}}$ and $\langle S_i S_j \rangle_{\tilde{P}}$ are the mean and correlation with respect to distribution \tilde{P} (Eq. (6)) and given by

$$\langle S_i \rangle_{\tilde{P}} = \frac{1}{t_{\max}} \sum_{t=1}^{t_{\max}} \tanh \left[h_i + \sum_{\substack{j'=1 \\ j' \neq i}}^N J_{ij'} S_{j'}(t) \right] \quad (9)$$

and

$$\langle S_i S_j \rangle_{\tilde{P}} = \frac{1}{t_{\max}} \sum_{t=1}^{t_{\max}} S_j(t) \tanh \left[h_i + \sum_{\substack{j'=1 \\ j' \neq i}}^N J_{ij'} S_{j'}(t) \right], \quad (10)$$

respectively. It should be noted that this updating rule avoids the calculation of $\langle S_i \rangle$ and $\langle S_i S_j \rangle$ with the original spin system, Eqs. (1) and (2), which is computationally formidable with $N = 264$. As $t_{\max} \rightarrow \infty$, the estimator obtained by the PL maximization approaches the exact maximum likelihood estimator⁷⁰. In fact, the Ising model with the estimated parameter values $\mathbf{h} = \hat{\mathbf{h}}$ and $\mathbf{J} = \hat{\mathbf{J}}$ produced the mean and correlation of spins in the empirical data with a sufficiently high accuracy (Supplementary Fig. 8).

We previously provided MATLAB code for estimating the Ising model from data by PL maximization³⁸. The code is publicly available on GitHub repository (<https://github.com/tkEzaki/energy-landscape-analysis>).

Monte Carlo simulation.

We used the Metropolis method⁷¹ to calculate the observables of the Ising model estimated from the empirical data and the SK model. In each time step, a spin S_i was chosen uniformly at random for being updated. The selected spin was flipped with probability $\min\{e^{-\Delta E}, 1\}$, where $\Delta E = E(\mathbf{S}_{\text{flipped}}) - E(\mathbf{S})$, \mathbf{S} is the current spin configuration, and $\mathbf{S}_{\text{flipped}}$ is the spin configuration after S_i is flipped. The initial condition was given by $S_i = 1$ with probability 1/2 (and hence $S_i = -1$ with probability 1/2), independently for different i 's. We recorded the spin configuration \mathbf{S} every N time steps.

For the empirical data, we discarded the first $10^6 \times N$ time steps as transient and then recorded 10^7 samples of \mathbf{S} in total. Based on the 10^7 samples, we calculated the averages of the observables (i.e., $|m|$, q , χ_{SG} , χ_{uni} , and C). For drawing the phase diagrams with the $N = 264$ ROIs, we further averaged each observable over 10 independent simulations starting from different initial spin configurations. In Fig. 1k, we averaged the χ_{SG} value over 40 combinations of N' ROIs out of the 264 ROIs as well as over 10^7 samples and 10 initial conditions.

For the phase diagram for the SK model, we discarded the first $10^4 \times N$ time steps as transient and then collected 5×10^4 samples of \mathbf{S} from each of 10^3 realizations of \mathbf{J} . We drew the phase diagrams on the basis of the $5 \times 10^4 \times 10^3 = 5 \times 10^7$ samples.

Estimation of μ and σ for single participants.

The estimation of the empirical interaction matrix, $\hat{\mathbf{J}}$, requires a large amount of data, or practically, concatenation of fMRI data across different participants. Therefore, one cannot directly compute the mean and standard deviation of $\hat{\mathbf{J}}$ (i.e., μ and σ) for each participant. Given this constraint, we estimated μ and σ for each participant (denoted by $\tilde{\mu}$ and $\tilde{\sigma}$) using the χ_{SG} and χ_{uni} values for the participant (denoted by $\tilde{\chi}_{\text{SG}}$ and $\tilde{\chi}_{\text{uni}}$) as follows (Supplementary Fig. 10).

First, we examined the phase diagrams in terms of χ_{SG} and χ_{uni} generated for the collection of all participants (Fig. 1c, d). Specifically, we calculated $\chi_{\text{SG}}(\mu, \sigma)$ and $\chi_{\text{uni}}(\mu, \sigma)$ values at $\mu = \mu_k$ ($k = 1, \dots, 25$), where $\mu_1 = -0.002$, $\mu_2 = -0.0015$, \dots , $\mu_{25} = 0.01$, and $\sigma = \sigma_\ell$ ($\ell = 1, \dots, 21$), where $\sigma_1 = 0$, $\sigma_2 = 0.0075$, \dots , $\sigma_{21} = 0.15$.

Second, at each μ_k ($k = 1, \dots, 25$), we computed the value of $\check{\sigma}_k$ satisfying $\chi_{\text{SG}}(\mu_k, \check{\sigma}_k) = \tilde{\chi}_{\text{SG}}$ (Supplementary Fig. 10a, c) using a linear interpolation of $\chi_{\text{SG}}(\mu_k, \sigma_\ell)$ ($\ell = 1, \dots, 21$), i.e., $\check{\sigma}_k = \alpha \sigma_{\ell'} + (1 - \alpha) \sigma_{\ell'+1}$, where ℓ' ($1 \leq \ell' \leq 21$) is the integer satisfying $\chi_{\text{SG}}(\mu_k, \sigma_{\ell'}) \leq \tilde{\chi}_{\text{SG}} < \chi_{\text{SG}}(\mu_k, \sigma_{\ell'+1})$, and $\alpha = [\chi_{\text{SG}}(\mu_k, \sigma_{\ell'+1}) - \tilde{\chi}_{\text{SG}}] / [\chi_{\text{SG}}(\mu_k, \sigma_{\ell'+1}) - \chi_{\text{SG}}(\mu_k, \sigma_{\ell'})]$. Because $\chi_{\text{SG}}(\mu_k, \sigma_\ell)$ increases with ℓ in the paramagnetic phase, the ℓ' value is uniquely determined for each k , if it exists. In this manner, we obtained a piecewise linear curve whose knots were $(\mu_k, \check{\sigma}_k)$ ($k = 1, \dots, 25$). On this curve, $\chi_{\text{SG}}(\mu, \sigma)$ is approximately equal to $\tilde{\chi}_{\text{SG}}$ (Supplementary Fig. 10e, g). It should be noted that we have assumed that $(\tilde{\mu}, \tilde{\sigma})$ to be estimated is near $(\hat{\mu}, \hat{\sigma})$ computed for the entire population (represented by the cross in Fig. 1a–d). More precisely, we are searching $(\tilde{\mu}, \tilde{\sigma})$ in the vicinity of the paramagnetic-SG phase boundary on the paramagnetic side. This assumption is supported by the empirical values of m and q for individual participants, i.e., $m = -8.0 \times 10^{-3} \pm 7.8 \times 10^{-3}$ (mean \pm SD) and $q = 3.4 \times 10^{-3} \pm 0.4 \times 10^{-3}$.

Third, we calculated a piecewise linear curve on which $\chi_{\text{uni}}(\mu, \sigma)$ was approximately equal to $\tilde{\chi}_{\text{uni}}$ (Supplementary Fig. 10f, g). To this end, we applied the same algorithm as the one used in the previous step but by fixing σ_ℓ (Supplementary Fig. 10b) and finding $\check{\mu}_\ell$ (Supplementary Fig. 10d), exploiting the fact that $\chi_{\text{uni}}(\mu_k, \sigma_\ell)$ monotonically increases with μ in the paramagnetic phase.

Finally, we computed $(\tilde{\mu}, \tilde{\sigma})$ for the individual as the intersection of the two piecewise linear curves (Supplementary Fig. 10g).

Specific heat.

The specific heat is defined by

$$C = \frac{\langle E^2 \rangle - \langle E \rangle^2}{NT^2}, \quad (11)$$

where T is the temperature. We set $T = 1$ because we implicitly did so in Eqs. (1) and (2).

To compute C for each participant, we first drew a phase diagram for C in terms of μ and σ for the entire population (Supplementary Fig. 11a). The obtained phase diagram was similar to that for the SK model (Supplementary Fig. 11b). Then, we determined the C value for each participant as the point in the phase diagram corresponding to the (μ, σ) for the participant. Because the phase diagram for C is drawn for discrete values of μ and σ , we applied the standard bilinear interpolation to determine the C value corresponding to a given (μ, σ) .

Statistics and reproducibility.

Statistical tests were performed using SPSS 24.0. The details of each analysis are found in prior sections.

Reporting summary.

Further information on research design is available in the Nature Research Reporting Summary linked to this article.

Data availability

The data set used in this study (Nathan Kline Institute Rockland phase I Sample) is publicly available (http://fcon_1000.projects.nitrc.org/indi/pro/nki.html).

Code availability

The code used in this study is available upon request.

Acknowledgements

The authors would like to thank Yoshiyuki Kabashima for useful discussions. TE acknowledges the support provided through PRESTO, JST (No. JPMJPR16D2) and Kawarabayashi Large Graph Project, ERATO, JST. MS acknowledges the support provided through the European Commission (CIG618600) and JSPS (16H02053; 16H05959; 16H06406; 16KT0002). TW acknowledges supports from JSPS (18H06094), Yamaha Sports Challenge Fellowship, Fukuhara Fund for Applied Psychoeducation Research, and SENSHIN Medical Research Foundation. NM acknowledges the support provided through, CREST, JST (No. JPMJCR1304) and Kawarabayashi Large Graph Project, ERATO, JST, and EPSRC Institutional Sponsorship to the University of Bristol.

Author contributions statement

N.M. designed research; T.E., E.F.R., and N.M. contributed new analytic tools; T.E. and M.S. analyzed data; T.E., E.F.R., T.W., M.S., and N.M. performed research; T.E., T.W., M.S., and N.M. wrote the paper.

Additional information

Competing interests The authors declare no conflict of interest.

References

1. Legenstein, R., Maass, W. What makes a dynamical system computationally powerful? *New Directions in Statistical Signal Processing From Systems to Brain* (eds. Haykin, S., Principe, J.C., Sejnowski, T.J. & McWhirter, J.) 127–154 (MIT Press, Cambridge, 2007).
2. Chialvo, D. R. Emergent complex neural dynamics. *Nat. Phys.* **6**(10), 744–750 (2010).
3. Plenz, D. Neuronal avalanches and coherence potentials. *Eur. Phys. J. Spec. Top.* **205**(1), 95–115 (2012).

4. Mora, T., Bialek, W. Are biological systems poised at criticality? *J. Stat. Phys.* **144**(2), 268–302 (2011).
5. Yu, S., Yang, H., Shriki, O., & Plenz, D. Universal organization of resting brain activity at the thermodynamic critical point. *Front. Syst. Neurosci.* **7**, 42 (2013).
6. Tkačik, G., et al. Thermodynamics and signatures of criticality in a network of neurons. *Proc. Natl. Acad. Sci. USA* **112**(37), 11508–11513 (2015).
7. Touboul, J., Destexhe, A. Can power-law scaling and neuronal avalanches arise from stochastic dynamics? *PLOS ONE* **5**(2), e8982 (2010).
8. Botcharova, M., Farmer, S. F. & Berthouze, L. Power-law distribution of phase-locking intervals does not imply critical interaction. *Phys. Rev. E* **86**(5), 051920 (2012).
9. Hesse, J., Gross, T. Self-organized criticality as a fundamental property of neural systems. *Front. Syst. Neurosci.* **8**, 166 (2014).
10. Marković, D., Gros, C. Power laws and self-organized criticality in theory and nature. *Phys. Rep.* **536**(2), 41–74 (2014).
11. Beggs, J. M., Plenz, D. Neuronal avalanches in neocortical circuits. *J. Neurosci.* **23**(35), 11167–11177 (2003).
12. Beggs, J. M., The criticality hypothesis: How local cortical networks might optimize information processing. *Phil. Trans. R. Soc. A* **366**(1864), 329–343 (2008).
13. Marinazzo, D., et al. Information transfer and criticality in the Ising model on the human connectome. *PLOS ONE* **9**(4), e93616 (2014).
14. Bialek, W. Perspectives on theory at the interface of physics and biology. *Rep. Prog. Phys.* **81**(1), 012601 (2018).
15. Langton, C. G. Computation at the edge of chaos: phase transitions and emergent computation. *Physica D* **42**(1-3), 12–37 (1990).
16. Bertschinger, N., Natschläger, T. Real-time computation at the edge of chaos in recurrent neural networks. *Neural Comput.* **16**(7), 1413–1436 (2004).
17. Legenstein, R., Maass, W. Edge of chaos and prediction of computational performance for neural circuit models. *Neural Netw.* **20**(3), 323–334 (2007).
18. Kopell, N. J., Gritton, H. J., Whittington, M. A. & Kramer, M. A. Beyond the connectome: the dynamo. *Neuron* **83**(6), 1319–1328 (2014).
19. Rabinovich, M. I., Simmons, A. N. & Varona, P. Dynamical bridge between brain and mind. *Trends Cogn. Sci.* **19**(8), 453–461 (2015).
20. Watanabe, T., Rees, G. Brain network dynamics in high-functioning individuals with autism. *Nat. Commun.* **8**, 16048 (2017).
21. Ezaki, T., Sakaki, M., Watanabe, T. & Masuda, N. Age-related changes in the ease of dynamical transitions in human brain activity. *Hum. Brain Mapp.* **39**(6), 2673–2688 (2018).
22. Vidaurre, D., et al. Spontaneous cortical activity transiently organises into frequency specific phase-coupling networks. *Nat. Commun.* **9**, 2987 (2018).
23. Taghia, J., et al. Uncovering hidden brain state dynamics that regulate performance and decision-making during cognition. *Nat. Commun.* **9**, 2505 (2018).
24. Watanabe, T., Masuda, N., Megumi, F., Kanai, R. & Rees, G. Energy landscape and dynamics of brain activity during human bistable perception. *Nat. Commun.* **5**, 4765 (2014).
25. Calhoun, V. D., Miller, R., Pearlson, G. & Tulay, A. The chronnectome: time-varying connectivity networks as the next frontier in fMRI data discovery. *Neuron* **84**(2), 262–274 (2014).
26. Barbey, A. Network neuroscience theory of human intelligence. *Trends Cogn. Sci.* **22**(1), 8–20 (2018).
27. Tagliazucchi, E., Balenzuela, P., Fraiman, D. & Chialvo, D. R. Criticality in large-scale brain fMRI dynamics unveiled by a novel point process analysis. *Front. Physiol.* **3**, 15 (2012).
28. Shriki, O., et al. Neuronal avalanches in the resting MEG of the human brain. *J. Neurosci.* **33**(16), 7079–7090 (2013).
29. Stam, C. J. Nonlinear dynamical analysis of EEG and MEG: review of an emerging field. *Clin. Neurophysiol.* **116**(10), 2266–2301 (2005).
30. Fischer, K. H., Hertz, J. A. *Spin Glasses*. (Cambridge University Press, Cambridge, 1991).

31. Rizzo, T., Crisanti, A. Chaos in temperature in the Sherrington-Kirkpatrick model. *Phys. Rev. Lett.* **90**(13), 137201 (2003).
32. Bray, A. J., Moore, M. A. Chaotic nature of the spin-glass phase. *Phys. Rev. Lett.* **58**(1), 57–60 (1987).
33. Aspelmeier, T. Free-energy fluctuations and chaos in the Sherrington-Kirkpatrick model. *Phys. Rev. Lett.* **100**(11), 117205 (2008).
34. Schneidman, E., Berry, M. J., Segev, R. & Bialek, W. Weak pairwise correlations imply strongly correlated network states in a neural population. *Nature* **440**, 1007–1012 (2006).
35. Tkačik, G., Schneidman, E., Berry, M. J. & Bialek, W. Ising models for networks of real neurons. *arXiv q-bio/0611072* (2006).
36. Mora, T., Deny, S. & Marre, O. Dynamical criticality in the collective activity of a population of retinal neurons. *Phys. Rev. Lett.* **114**, 078105 (2015).
37. Watanabe, T., et al. A pairwise maximum entropy model accurately describes resting-state human brain networks. *Nat. Commun.* **4**, 1370 (2013).
38. Ezaki, T., Watanabe, T., Ohzeki, M. & Masuda, N. Energy landscape analysis of neuroimaging data. *Phil. Trans. R. Soc. A* **375**(2096), 20160287 (2017).
39. Blair, C. How similar are fluid cognition and general intelligence: a developmental neuroscience perspective on fluid cognition as an aspect of human cognitive ability. *Behav. Brain Sci.* **29**(2), 109–160 (2006).
40. Ree, M. J., Earles, J. A. Intelligence is the best predictor of job performance. *Curr. Dir. Psychol. Sci.* **1**(3), 86–89 (1992).
41. Power, J. D., et al. Functional network organization of the human brain. *Neuron* **72**(4), 665–678 (2011).
42. Wechsler, D. *Wechsler Abbreviated Scale of Intelligence*. (The Psychological Corporation, San Antonio, 1999).
43. McCrimmon, A. W., Smith, A. D. Review of the Wechsler Abbreviated Scale of Intelligence, second edition (WASI-II). *J. Psychoeduc. Assess.* **31**(3), 337–341 (2013).
44. Weaver, B., Wuensch, K. L. SPSS and SAS programs for comparing Pearson correlations and OLS regression coefficients. *Behav. Res. Methods* **45**(3), 880–895 (2013).
45. Tukey, J. W. *Exploratory Data Analysis*. (Addison-Wesley, Massachusetts, 1977).
46. Kanji, G. K. *100 Statistical Tests*. (SAGE Publications, London, 2006).
47. Kantelhardt, J. W., Koscielny-Bunde, E., Rego, H. H., Havlin, S. & Bunde, A. Detecting long-range correlations with detrended fluctuation analysis. *Physica A* **295**(3-4), 441–454 (2001).
48. Tagliazucchi, E., et al. Large-scale signatures of unconsciousness are consistent with a departure from critical dynamics. *J. R. Soc. Interface* **13**(114), 20151027 (2016).
49. Deary, I. J., Penke, L. & Johnson, W. The neuroscience of human intelligence differences. *Nat. Rev. Neurosci.* **11**, 201–211 (2010).
50. Meisel, C., Bailey, K., Achermann, P. & Plenz, D. Decline of long-range temporal correlations in the human brain during sustained wakefulness. *Sci. Rep.* **7**, 11825 (2017).
51. Horne, J. A. Sleep loss and ‘divergent’ thinking ability. *Sleep* **11**(6), 528–536 (1988).
52. Song, M., et al. Brain spontaneous functional connectivity and intelligence. *Neuroimage* **41**(3), 1168–1176 (2008).
53. van den Heuvel, M. P., Stam, C. J., Kahn, R. S., Hulshoff, Pol, H. E. Efficiency of functional brain networks and intellectual performance. *J. Neurosci.* **29**(23), 7619–7624 (2009).
54. Cole, M. W., Yarkoni, T., Repovs, G., Anticevic, A. & Braver, T. S. Global connectivity of prefrontal cortex predicts cognitive control and intelligence. *J. Neurosci.* **32**(26), 8988–8999 (2012).
55. Finn, E. S., et al. Functional connectome fingerprinting: identifying individuals using patterns of brain connectivity. *Nat. Neurosci.* **18**, 1664–1671 (2015).
56. Song, M. et al. Default network and intelligence difference. *IEEE Trans. Auton. Mental. Develop.* **1**, 101–109 (2009).
57. Chen, X., Randi, F., Leifer, A. M. & Bialek, W. Searching for collective behavior in a small brain. *Phys. Rev. E* **99**, 052418 (2014).
58. Tkačik, G., et al. Searching for collective behavior in a large network of sensory neurons. *PLOS Comput. Biol.* **10**, e1003408 (2014).

59. Shew, W. L., Yang, H., Petermann, T., Roy, R. & Plenz, D. Neuronal avalanches imply maximum dynamic range in cortical networks at criticality. *J. Neurosci.* **29(49)**, 15595–15600 (2009).
60. Kinouchi, O., Copelli, M. Optimal dynamical range of excitable networks at criticality. *Nat. Phys.* **2**, 348–352 (2006).
61. Haimovici, A., Tagliazucchi, E., Balenzuela, P. & Chialvo, D. R. Brain organization into resting state networks emerges at criticality on a model of the human connectome. *Phys. Rev. Lett.* **110**, 178101 (2013).
62. Deco, G., Jirsa, V. K. Ongoing cortical activity at rest: criticality, multistability, and ghost attractors. *J. Neurosci.* **32(10)**, 3366–3375 (2012).
63. Fraiman, D., Balenzuela, P., Foss, J. & Chialvo, D. R. Ising-like dynamics in large-scale functional brain networks. *Phys. Rev. E* **79(6)**, 061922 (2009).
64. Kitzbichler, M. G., Smith, M. L., Christensen, S. R. & Bullmore, E. Broadband criticality of human brain network synchronization. *PLOS Comput. Biol.* **5(3)**, e1000314 (2009).
65. Hahn, G., et al. Spontaneous cortical activity is transiently poised close to criticality. *PLOS Comput. Biol.* **13(5)**, 1005543 (2017).
66. Priesemann, V., et al. Spike avalanches in vivo suggest a driven, slightly subcritical brain state. *Front. Syst. Neurosci.* **8**, 108 (2014).
67. Bishop, C. M. *Pattern Recognition and Machine Learning* (Springer, New York, 2006).
68. Nooner, K. B., et al. The NKI-Rockland sample: a model for accelerating the pace of discovery science in psychiatry. *Front. Neurosci.* **6**, 152 (2012).
69. Masuda, N., Sakaki, M., Ezaki, T. & Watanabe, T. Clustering coefficients for correlation networks. *Front. Neuroinform.* **12**, 7 (2018).
70. Besag, J. Statistical analysis of non-lattice data. *J. R. Stat. Soc. D* **24(3)**, 179–195 (1975).
71. Chib, S., Greenberg, E. Understanding the Metropolis-Hastings algorithm. *Am. Stat.* **49(4)**, 327–335 (1995).

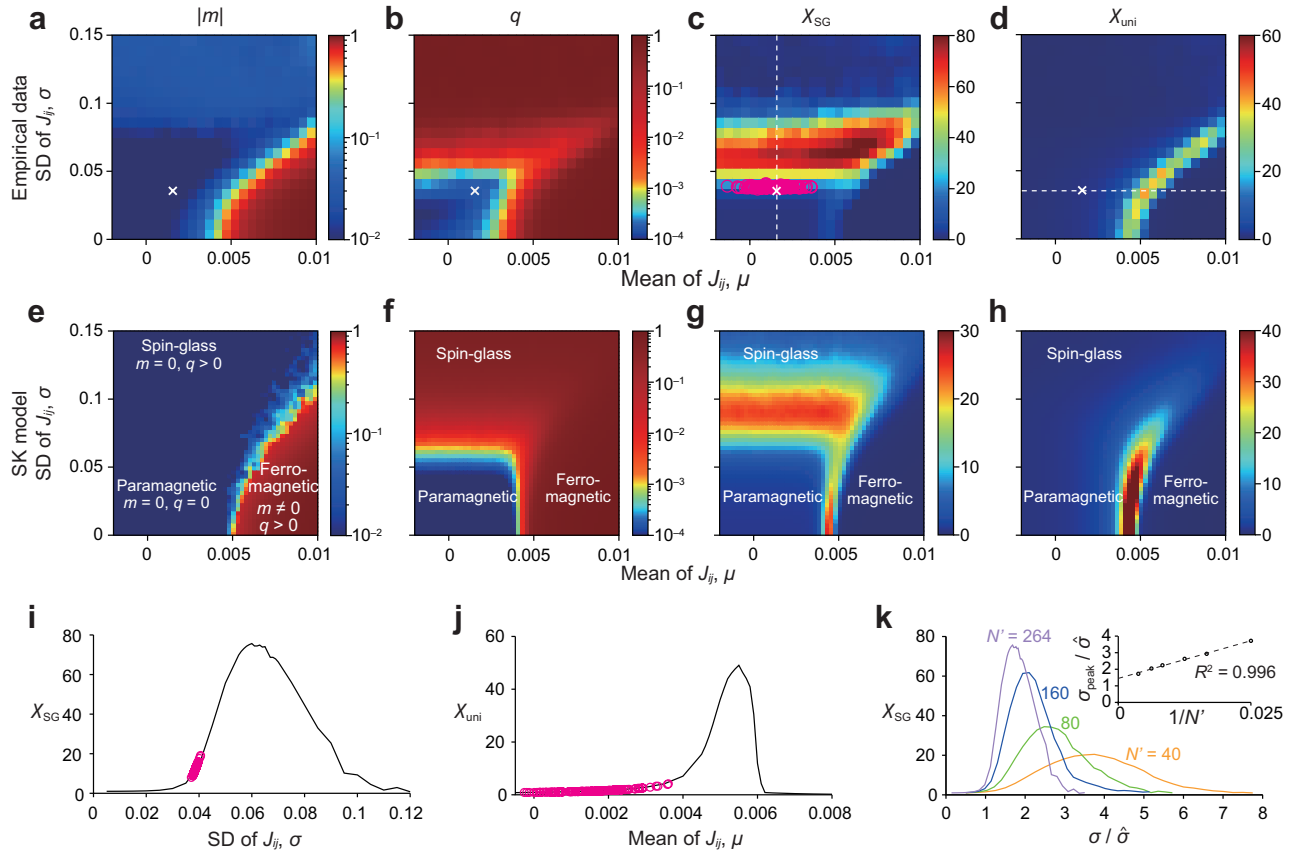


Figure 1. **a–d** Phase diagrams for the empirical data. **e–h** Phase diagrams for the SK model. **a, e:** $|m|$. **b, f:** q . **c, g:** χ_{SG} . **d, h:** χ_{uni} . In (**a, d**), the crosses represent the mean and standard deviation of the J_{ij} estimated for the entire population of the participants, i.e., $(\hat{\mu}, \hat{\sigma})$. In (**c**), a circle represents a participant. In (**a**) and (**e**), we plot $|m|$ instead of m . This is because averaging over simulations and over realizations of \mathbf{J} would lead to $m \approx 0$ due to symmetry breaking, even if $m \neq 0$ in theory such as in the ferromagnetic phase. **i** χ_{SG} as a function of σ , with $\mu = \hat{\mu}$ being fixed. **j** χ_{uni} as a function of μ , with $\sigma = \hat{\sigma}$ being fixed. In (**i**) and (**j**), the curves are the cross-sectional view of (**c**) and (**d**), respectively, along the dashed line in (**c**) or (**d**). The circles in (**i**) and (**j**) represent the individual participants and are the projection of the circles in (**c**) and (**d**) onto the dashed line. **k** Scaling behavior of χ_{SG} when the system size N' is varied. The value of $\sigma = \sigma_{peak}$ that maximizes χ_{SG} is plotted against $1/N'$ in the inset. The dashed line is the linear regression based on the six data points, $N' = 40, 60, 80, 120, 160$, and 264. The coefficient of determination is denoted by R^2 .

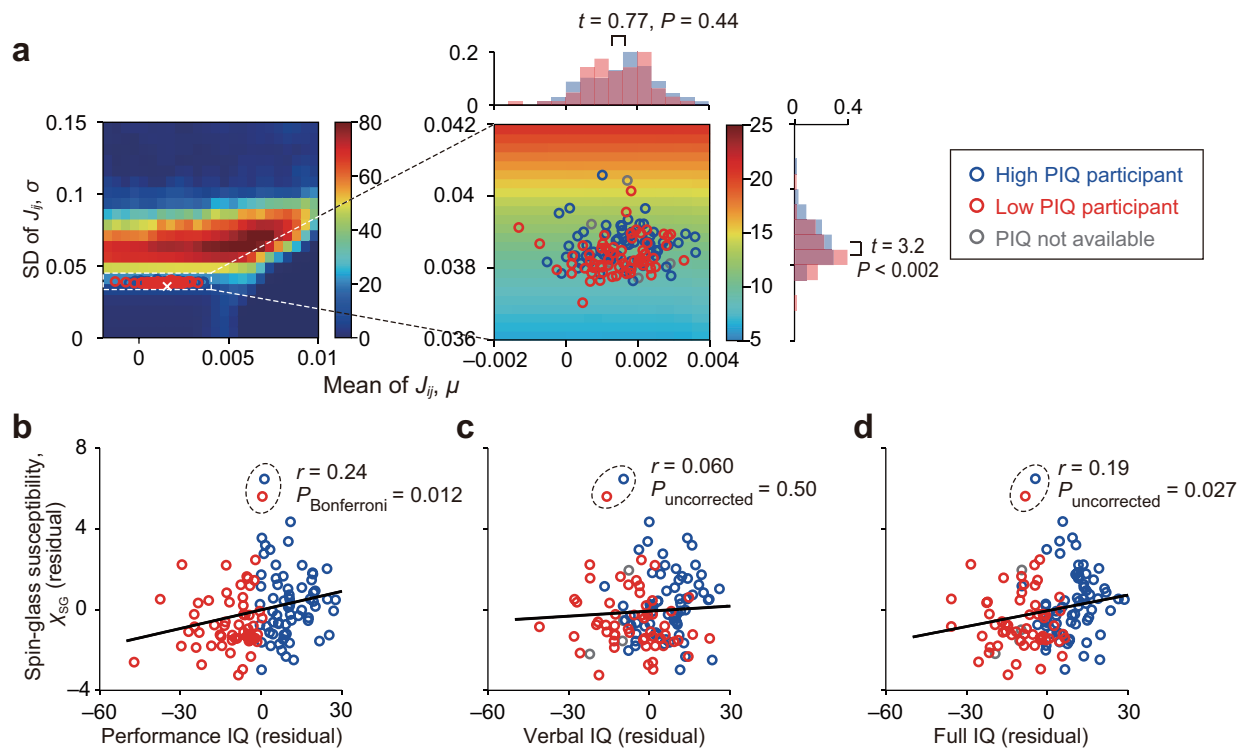
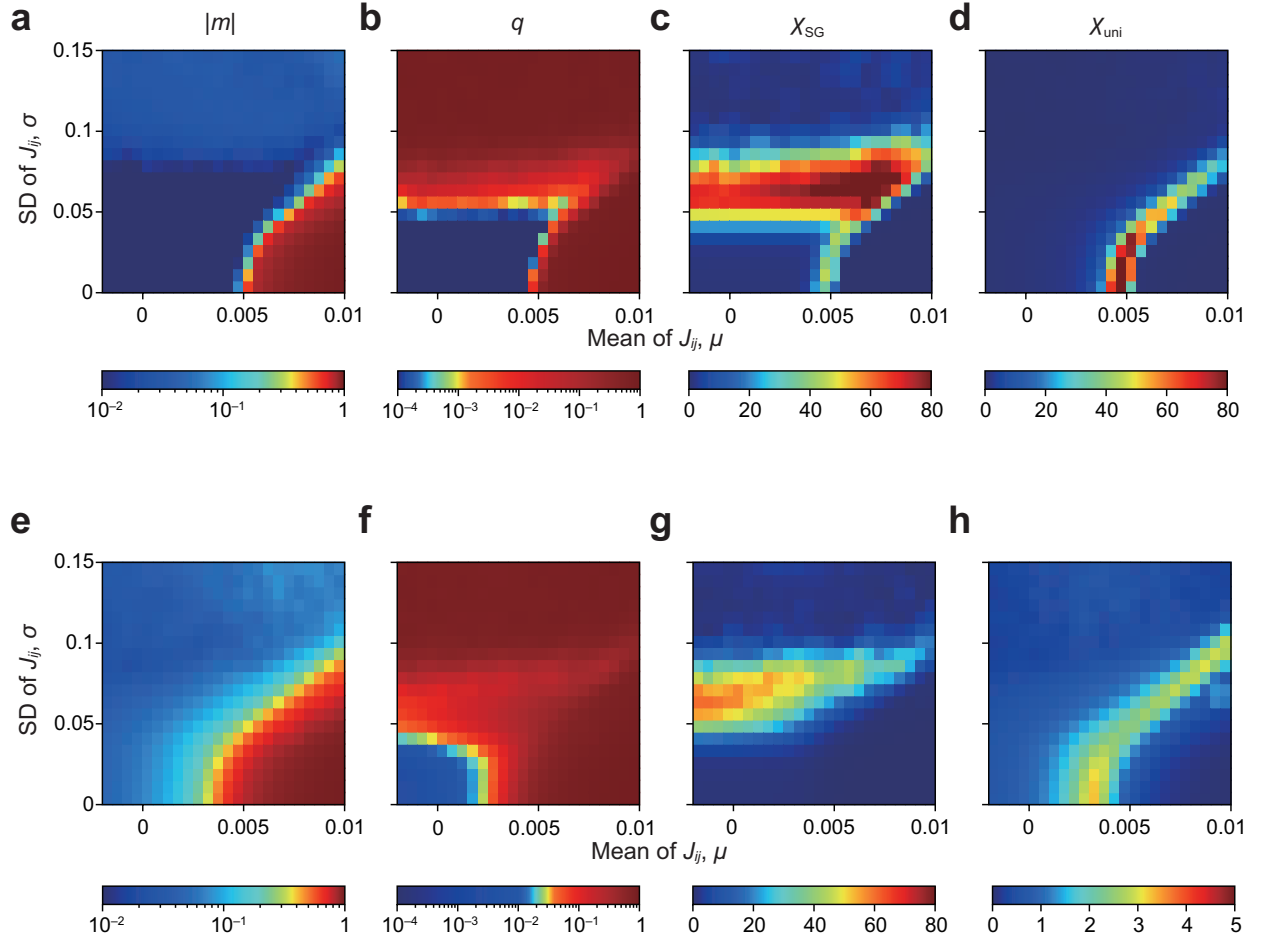
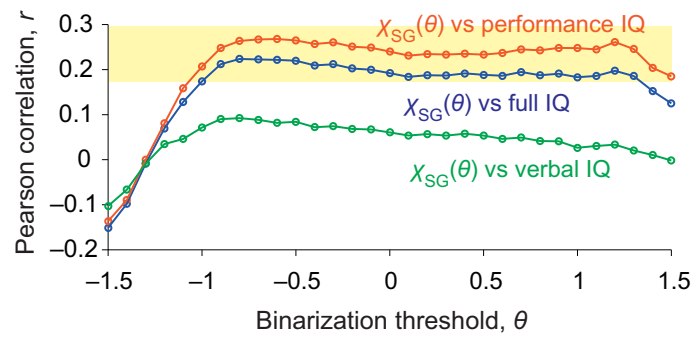


Figure 2. Association between the spin-glass susceptibility and the IQ scores. **a** Magnification of Fig. 1c. The blue and red circles represent participants with a high performance IQ score (≥ 109) and a low performance IQ score (< 109), respectively. The two overlapping histograms on the horizontal axis are the distributions of $\bar{\mu}$ for each participant group. The histograms on the vertical axis are the distributions of $\bar{\sigma}$. **b** Relationship between χ_{SG} and the performance IQ. A solid circle represents a participant. The participants enclosed by the dashed circle represent outliers determined by Tukey's 1.5 quartile criteria⁴⁵. The Pearson correlation value (i.e., r) and the P value shown in the figure are those calculated in the presence of the outliers. The solid line is the linear regression. **c** Relationship between χ_{SG} and the verbal IQ. **d** Relationship between χ_{SG} and the full IQ. The χ_{SG} and IQ values shown in (b), (c), and (d) are those after the effects of the age and the gender have been partialled out.

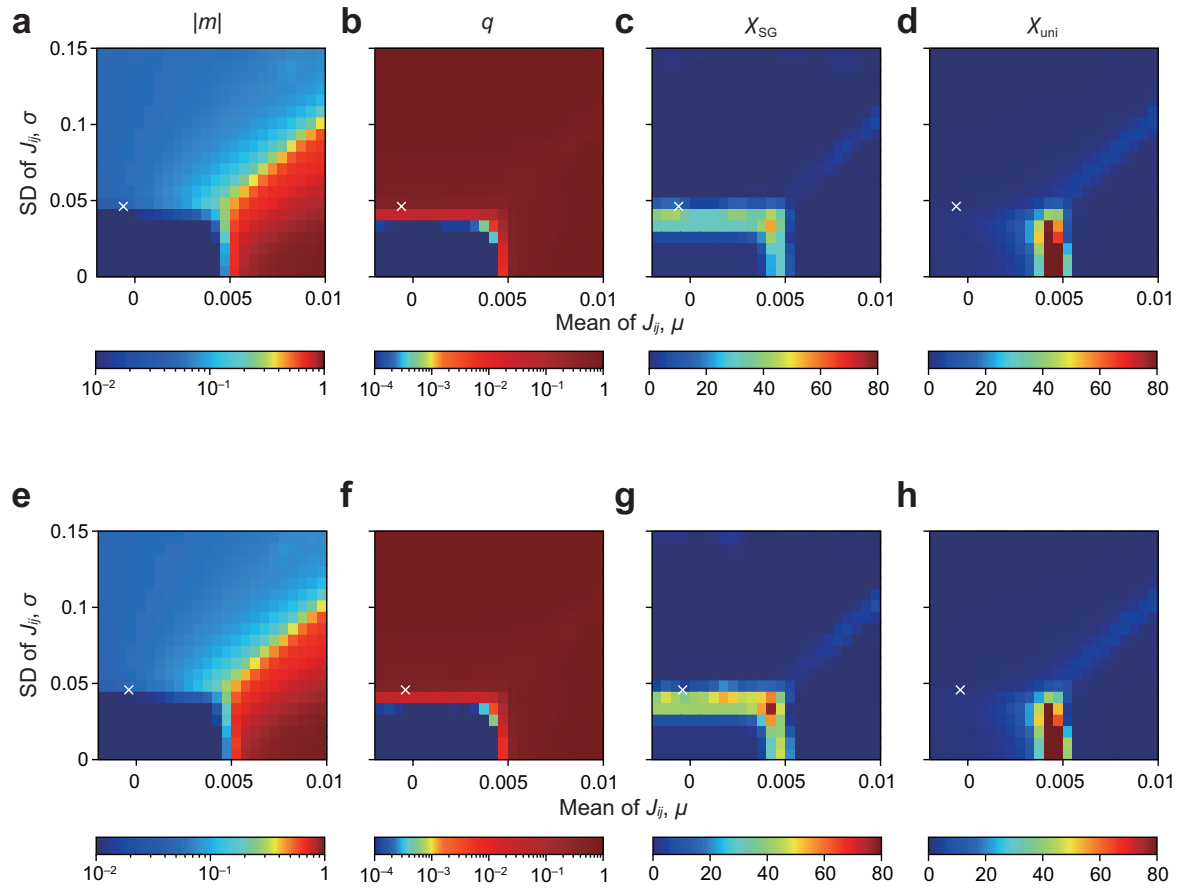
Supplementary Figures



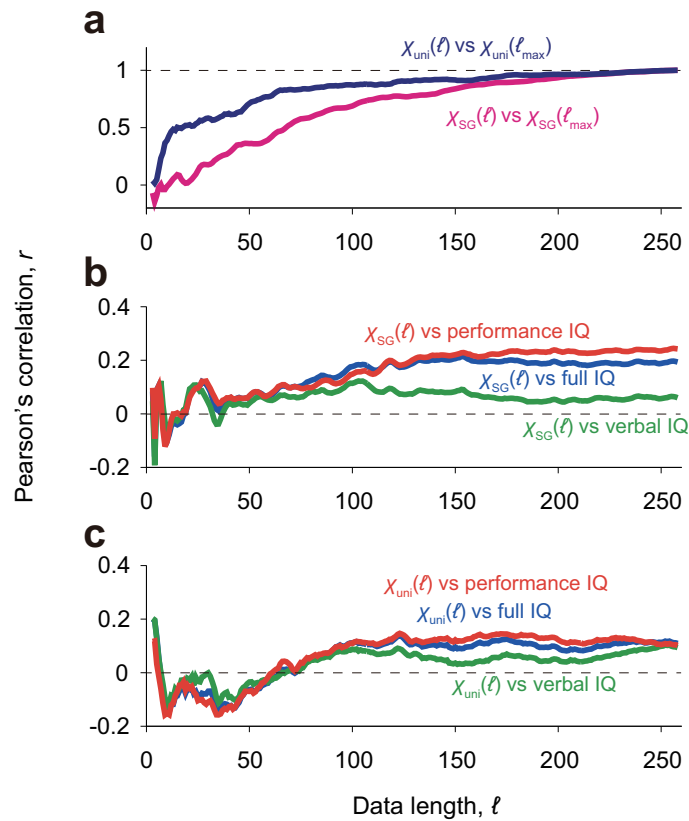
Supplementary Figure 1. Robustness of phase diagrams for the empirical data against variations in h . **(a–d)** $h_i = 0$ ($i = 1, \dots, N$). **(a–d)** $h_i = 2 \times \max_{1 \leq i' \leq N} \hat{h}_{i'}$ ($i = 1, \dots, N$). **a, e**: $|m|$. **b, f**: q . **c, g**: χ_{SG} . **d, h**: χ_{uni} . Note that the phase diagrams when $h_i = -2 \times \max_{1 \leq i' \leq N} \hat{h}_{i'}$ ($i = 1, \dots, N$) are the same as **(e–h)** owing to the symmetry. Therefore, given that **(a–d)** are qualitatively similar to **(e–h)**, we expect that h_i values satisfying $-2 \times \max_{1 \leq i' \leq N} \hat{h}_{i'} \leq h_i \leq 2 \times \max_{1 \leq i' \leq N} \hat{h}_{i'}$ produce qualitatively the same phase diagrams.



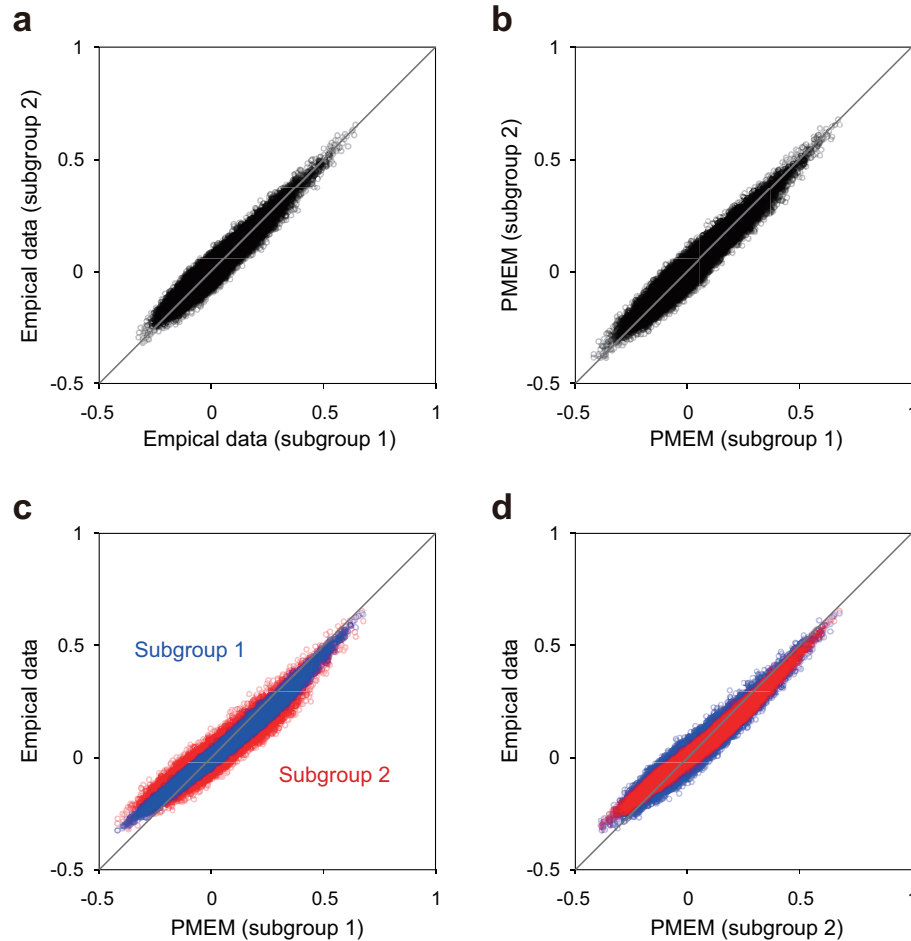
Supplementary Figure 2. Correlations between the IQ scores and $\chi_{SG}(\theta)$ when the binarization threshold (i.e., θ) is varied between -1.5 and 1.5 . We set $S_i(t) = +1$ if $z_i(t) \geq \theta$ and $S_i(t) = -1$ otherwise, extending Eq. (4) in the main text. As a guideline, with $\theta = -1$ and $\theta = 1$, the fraction of $S_i = +1$ is ≈ 0.853 and ≈ 0.148 , respectively. The shaded area represents $P < 0.05$. Outliers were not removed in this analysis.



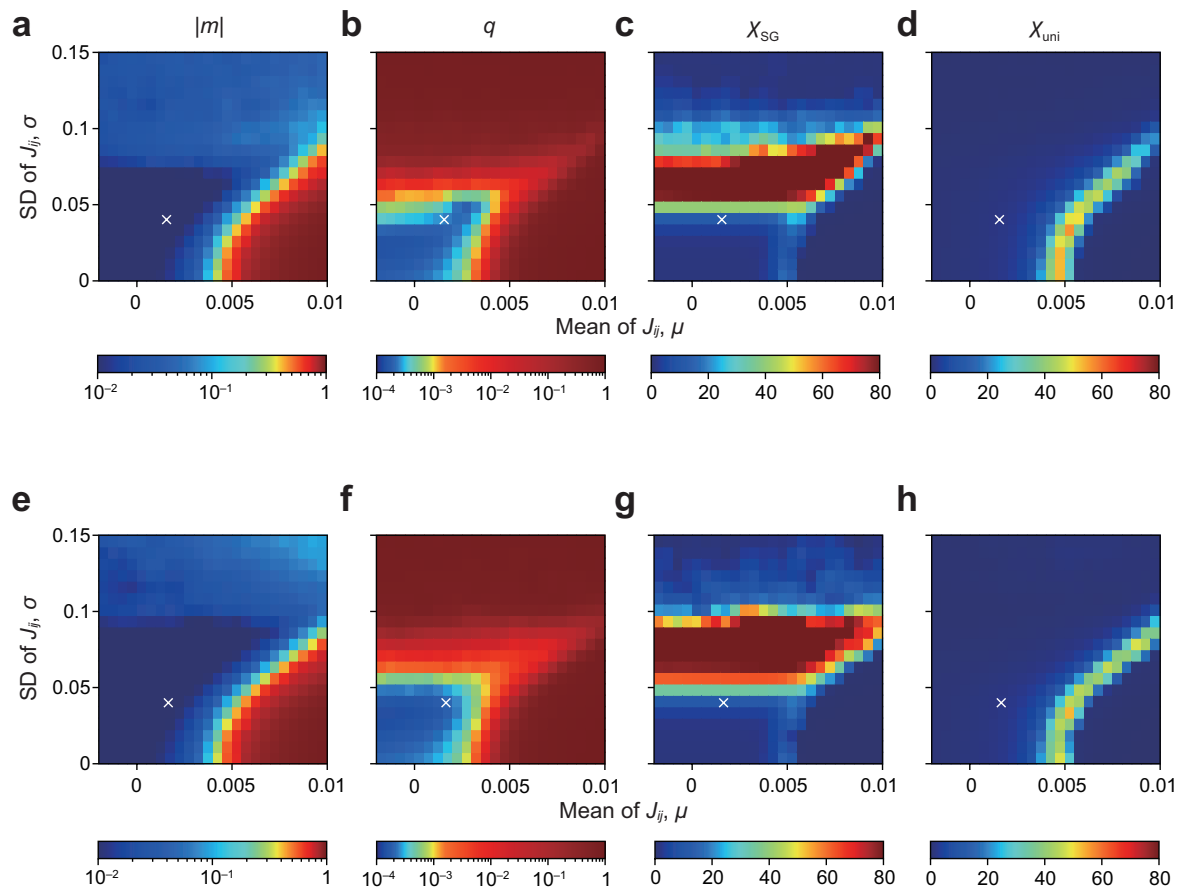
Supplementary Figure 3. Phase diagrams with different thresholds for binarization. We set $\theta = 1$ in (a–d) and $\theta = -1$ in (e–h). **a** and **e**: $|m|$. **b** and **f**: q . **c** and **g**: χ_{SG} . **d** and **h**: χ_{uni} .



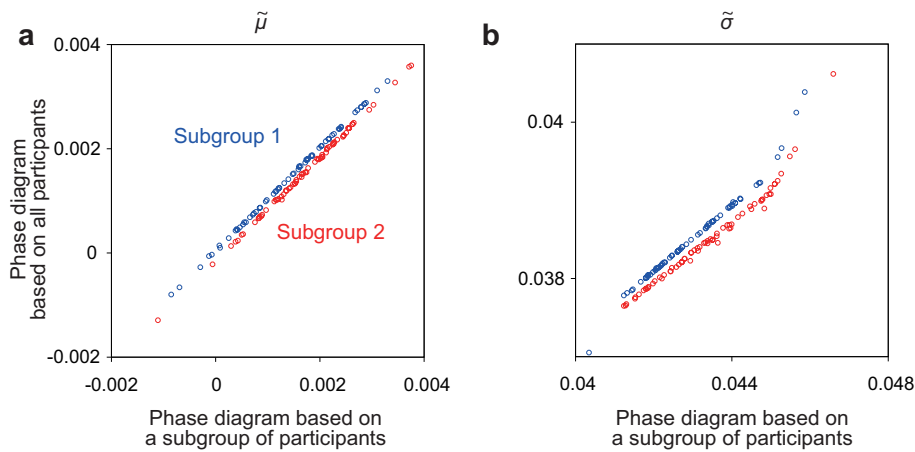
Supplementary Figure 4. Robustness of the spin-glass and uniform susceptibilities for the individual participants. We first computed χ_{SG} and χ_{uni} for each participant using the first ℓ volumes, and denote them by $\chi_{\text{SG}}(\ell)$ and $\chi_{\text{uni}}(\ell)$, respectively. For $\ell = \ell_{\text{max}} = 258$, these values (i.e., $\chi_{\text{SG}}(\ell_{\text{max}})$ and $\chi_{\text{uni}}(\ell_{\text{max}})$) coincide with the SG and uniform susceptibilities reported in the main text. **a** Pearson's correlation coefficient between $\chi_{\text{SG}}(\ell)$ and $\chi_{\text{SG}}(\ell_{\text{max}})$ and between $\chi_{\text{uni}}(\ell)$ and $\chi_{\text{uni}}(\ell_{\text{max}})$. **b** Pearson's correlation coefficient between $\chi_{\text{SG}}(\ell)$ and IQ scores. **c** Pearson's correlation coefficient between $\chi_{\text{uni}}(\ell)$ and IQ scores. To calculate the correlation coefficient, we regarded each participant as a sample.



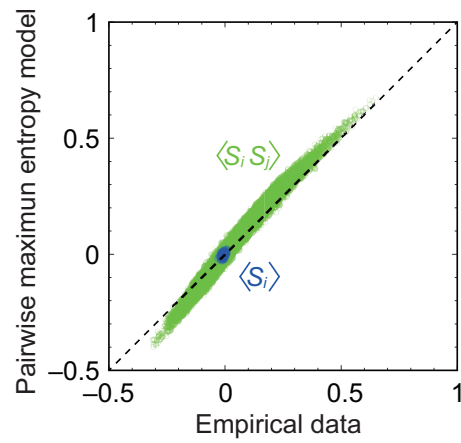
Supplementary Figure 5. Robustness of spin correlation, $\langle S_i S_j \rangle$, with respect to the grouping of participants. We split the participants into two halves, such that each subgroup of participants contains randomly selected 69 participants. **a** Comparison between $\langle S_i S_j \rangle$ directly calculated for the empirical data obtained from the first subgroup of participants and that for the second subgroup. A circle represents a pair of i and j ($1 \leq i < j \leq N$). **b** Comparison between $\langle S_i S_j \rangle$ calculated for the PMEM that we estimated for the first subgroup and that for the second subgroup. **c** Comparison between $\langle S_i S_j \rangle$ calculated for the PMEM that we estimated for the first subgroup, shown on the horizontal axis, and $\langle S_i S_j \rangle$ directly calculated for the first or second subgroup of the empirical data, shown on the vertical axis. **d** Comparison between $\langle S_i S_j \rangle$ calculated for the PMEM that we estimated for the second subgroup and $\langle S_i S_j \rangle$ directly computed for the first or second subgroup of the empirical data. The solid lines represent the diagonal.



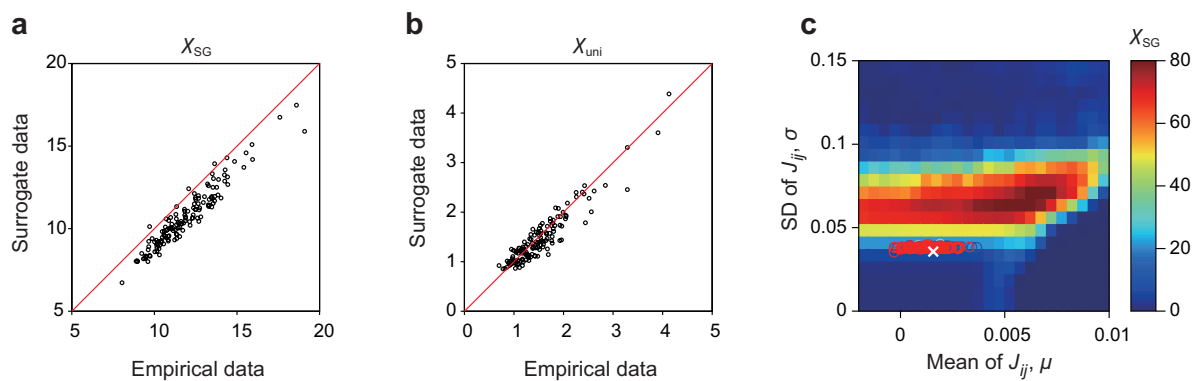
Supplementary Figure 6. Phase diagrams for each half of the participants. **a–d** Phase diagrams for the first subgroup of 69 participants used in Supplementary Fig. 5. **e–h** Phase diagrams for the second subgroup of 69 participants used in Supplementary Fig. 5. **a, e**: $|m|$. **b, f**: q . **c, g**: χ_{SG} . **d, h**: χ_{uni} . The crosses represent the mean and standard deviation of the J_{ij} estimated for the corresponding subgroup.



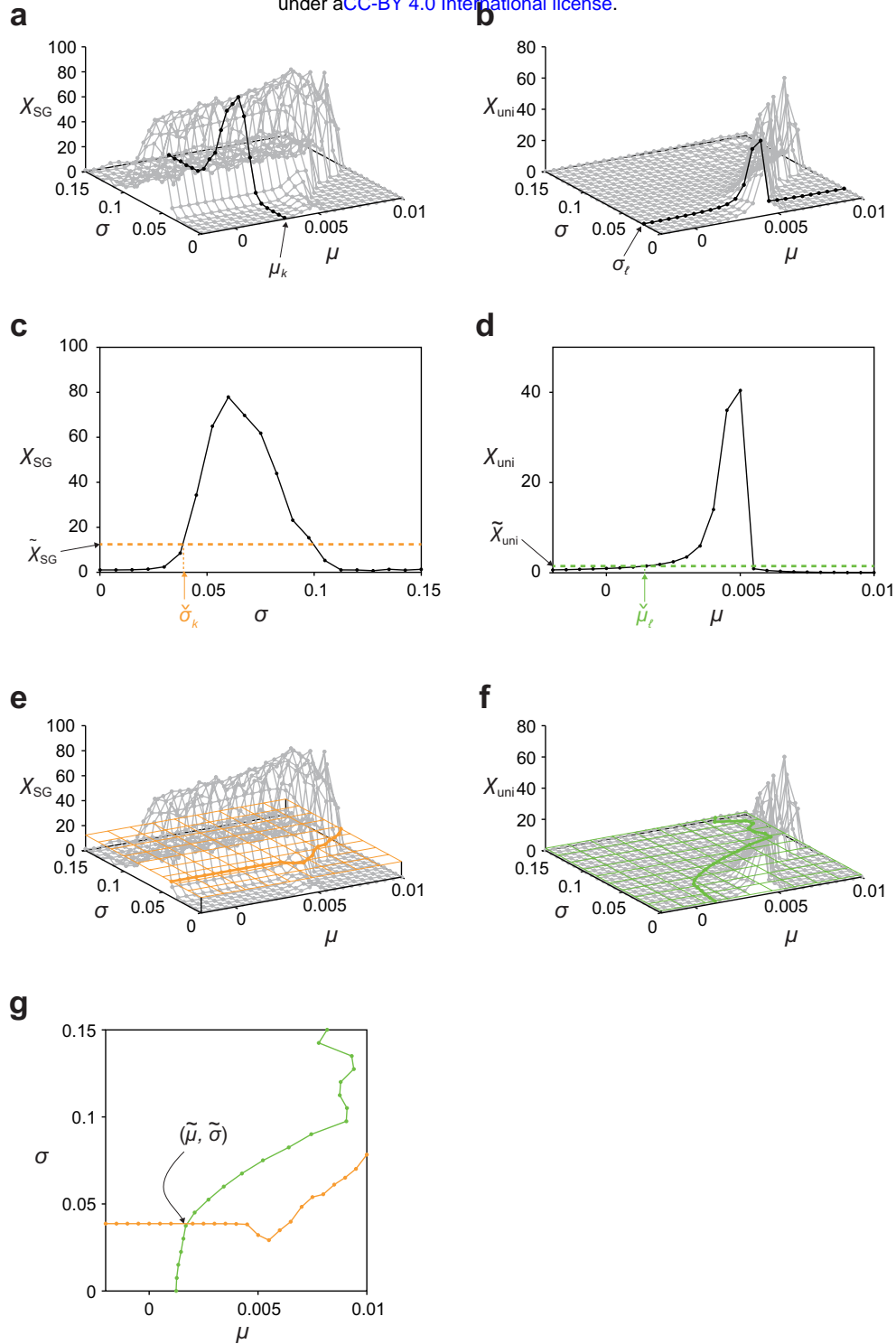
Supplementary Figure 7. Robustness of estimating $\tilde{\mu}$ and $\tilde{\sigma}$ for the individual participants. For each participant in each subgroup used in Supplementary Figs. 5 and 6, we computed $\tilde{\mu}$ (**a**) and $\tilde{\sigma}$ (**b**) using the phase diagrams of the corresponding subgroup composed of a half of the participants (i.e., 69 participants). Then, we compared the $\tilde{\mu}$ and $\tilde{\sigma}$ values thus calculated for the participant with those for the same participant computed using the phase diagrams based on all the participants (i.e., Fig. 1c,d in the main text). Each circle represents a participant. In (**b**), $\tilde{\sigma}$ estimated based on half the participants is consistently larger than that estimated based on all participants. This is because transition from the paramagnetic phase to the SG phase starts earlier (i.e., relevant order parameters start to increase) when all the participants are used as compared to when half the participants are used. This is considered to be a finite size effect in terms of the length of the data. However, we consider that this effect is not detrimental to our main results because, as shown in (**b**), the rank of the participants in terms of the $\tilde{\sigma}$ value is preserved with a high accuracy between the two cases.



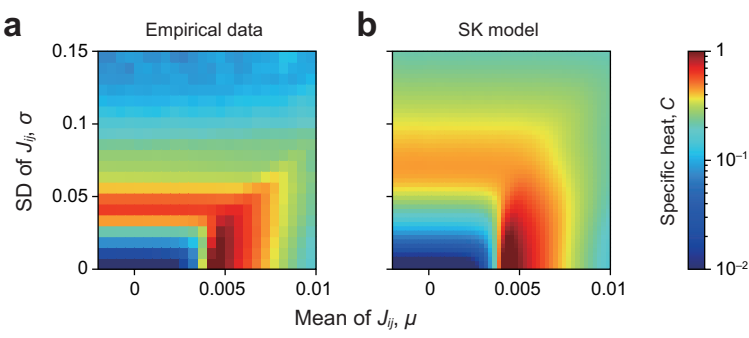
Supplementary Figure 8. Accuracy of the PL maximization. We compared $\langle S_i \rangle$ and $\langle S_i S_j \rangle$ between the empirical data and PMEM. Each circle represents an i value for $\langle S_i \rangle$ and an (i, j) pair for $\langle S_i S_j \rangle$. We set $h_i = 0$ ($i = 1, \dots, N$) in the simulations. The results for PMEM were obtained by Monte Carlo simulations.



Supplementary Figure 9. Results obtained with surrogate data. **a** Comparison between χ_{SG} computed for the empirical data and that for the surrogate data. **b** Comparison between χ_{uni} computed for the empirical data and that for the surrogate data. **c** Distribution of the participants on the phase diagram computed for surrogate data (see also Fig. 2a in the main text). To obtain the surrogate data for each participant, we observed $t_{\max} = 2 \times 10^4$ samples from a multivariate Gaussian distribution having the same mean vector and covariance matrix as those for the empirical data. Each circle represents a participant. These results suggest that our main results are reproduced solely from the covariance structure in the empirical data.



Supplementary Figure 10. Procedure for determining the μ and σ values for the individual participants. **a** Piecewise linear approximation of χ_{SG} as a function of σ for a given $\mu = \mu_k$. **b** Piecewise linear approximation of χ_{uni} as a function of μ for a given $\sigma = \sigma_\ell$. **c** By restricting oneself to the paramagnetic phase, one can identify the value of σ , denoted by $\check{\sigma}_k$, that realizes $\chi_{SG}(\mu_k, \check{\sigma}_k) \approx \tilde{\chi}_{SG}$. **d** By restricting oneself to the paramagnetic phase, one can identify the value of μ , denoted by $\check{\mu}_\ell$, that realizes $\chi_{uni}(\check{\mu}_\ell, \sigma_\ell) \approx \tilde{\chi}_{uni}$. **e** By connecting $(\mu_k, \check{\sigma}_k)$ by a piecewise linear curve, we obtain a curve on which $\chi_{SG} \approx \tilde{\chi}_{SG}$. **f** By connecting $(\check{\mu}_\ell, \sigma_\ell)$ by a piecewise linear curve, we obtain a curve on which $\chi_{uni} \approx \tilde{\chi}_{uni}$. **g** The intersection of the piecewise linear curves plotted in (e) and (f) yields the estimate of the μ and σ values for a single participant, denoted by $\tilde{\mu}$ and $\tilde{\sigma}$.



Supplementary Figure 11. Specific heat. **a** Empirical data, calculated for the entire population of the participants. **b** SK model.